Journal of Magnetic Resonance 263 (2016) 92–100

Contents lists available at ScienceDirect

Journal of Magnetic Resonance

journal homepage: www.elsevier.com/locate/jmr

Communication

Constant-variable flip angles for hyperpolarized media MRI

He Deng [a,b], Jianping Zhong [a], Weiwei Ruan [a], Xian Chen [a], Xianping Sun [a], Chaohui Ye [a], Maili Liu [a], Xin Zhou [a,*]

[a] State Key Laboratory of Magnetic Resonance and Atomic and Molecular Physics, National Center for Magnetic Resonance in Wuhan, Wuhan Institute of Physics and Mathematics, Chinese Academy of Sciences, Wuhan 430071, China
[b] The Department of Information Technology, Central China Normal University, Wuhan 430079, China

ARTICLE INFO

Article history:
Received 7 July 2015
Revised 10 December 2015
Available online 7 January 2016

Keywords:
Hyperpolarized MRI
Constant flip angles
Constant-variable flip angles
Variable flip angles

ABSTRACT

The longitudinal magnetization of hyperpolarized media, such as hyperpolarized ^{129}Xe, ^{3}He, etc., is nonrenewable. When the MRI data acquisition begins at the *k*-domain center, a constant flip angle (CFA) results in an image of high signal-to-noise ratio (SNR) but sacrifices the accuracy of spatial information. On the other hand, a variable flip angle (VFA) strategy results in high accuracy but suffers from a low SNR. In this paper, we propose a novel scheme to optimize both the SNR and accuracy, called constant-variable flip angles (CVFA). The proposed scheme suggests that hyperpolarized magnetic resonance signals are firstly acquired through a train of n^* CFA excitation pulses, followed by a train of N–n^* VFA excitation pulses. We simulate and optimize the flip angle used in the CFA section, the number of CFA excitation pulses, the number of VFA excitation pulses, and the initial and final variable flip angles adopted in the VFA section. Phantom and *in vivo* experiments demonstrate the good performance of the CVFA designs and their ability to maintain both high SNR and spatial resolution.

1. Introduction

Hyperpolarized noble gases (^{3}He and ^{129}Xe) provide a distinctive and noninvasive contrast mechanism in both static and dynamic MRI of the lungs [1–9]. Through laser optical pumping techniques, i.e., spin-exchange optical pumping (SEOP), the polarization levels can be amplified up to 10^{3}–10^{5} times above thermal equilibrium levels [3]. Under these conditions, hyperpolarized ^{129}Xe or ^{3}He MRI makes imaging of both pulmonary ventilation and diffusion feasible. Because ^{129}Xe can dissolve in blood and tissues, it enables evaluation of the pulmonary function of gas-blood exchange, whereas such measurement is not possible with ^{3}He [8,9]. Nevertheless, such nonequilibrium polarizations are not renewable: apart from normal relaxation processes, the available hyperpolarized magnetization gradually decays with each radio frequency (RF) excitation pulse [10]. The rapid losses of nonrenewable polarization necessitate more efficient imaging methods that maximize signal-to-noise ratio (SNR). This limited SNR problem is particularly acute for experiments constrained to a single breath hold time.

Besides SEOP, other hyperpolarization methods, such as dynamic nuclear polarization (DNP) [11,12], parahydrogen induced polarization (PHIP) [13], metastability exchange optical pumping (MEOP) [14], and chemically induced dynamic nuclear polarization (CIDNP) [15], have been explored as tools to enhance nuclear polarization in a wide range of (often complementary) applications [16,17]. Dynamic nuclear polarization is mostly performed at low temperature (≈1 k) and high magnetic field (≈3 T), and can polarize compounds containing NMR-sensitive nuclei, such as ^{13}C or ^{15}N, for *in vivo* metabolic imaging and other applications. Parahydrogen induced polarization involves enrichment of hydrogen in the para state, which is typically transferred to unsaturated molecules by reacting the hydrogen molecules with a precursor in the presence of a transition metal [18,19] or nanoparticle catalyst [20–22]. Metastability exchange optical pumping so far can only polarize ^{3}He nuclei at room temperature and at low pressures (≈a few mbars). Chemically induced dynamic nuclear polarization is the name given to the non-equilibrium nuclear spin state populations produced in chemical reactions that involve radicals. However, similar to the SEOP, the resulting polarization obtained from the DNP, PHIP, MEOP, or CIDNP method is independent of the main external magnetic field, but this polarization is also nonrenewable and has a limited lifetime [i.e., the longitudinal magnetization decays to thermal equilibrium value according to the spin–lattice relaxation time after each excitation pulse]. The unique characteristics of hyperpolarized magnetization make it difficult to achieve a high SNR while

* Corresponding author.
E-mail address: xinzhou@wipm.ac.cn (X. Zhou).

http://dx.doi.org/10.1016/j.jmr.2015.12.022
1090-7807/

maintaining high spatial resolution in the reconstructed MR images.

Owing to the rapid depletion of nonrenewable hyperpolarized longitudinal magnetization, smart strategies must be developed to make the most of the available polarization within the shortest possible time [23]. Small-angle-excitation methods, such as the constant-flip-angle (CFA) and variable-flip-angle (VFA) schemes, are particularly suitable for imaging hyperpolarized species due to improved efficiency in preserving the polarization during the sampling of many points in k-space [8–10,23–25]. The center of k-space has a low spatial frequency and represents the coarse features of the reconstructed image, while the edges of k-space have a high spatial frequency and characterize the fine details of the image. Previous research has compared the SNR and the resolution of boundaries of images of sealed cells of hyperpolarized ^{129}Xe acquired with sequential and centric phase-encoding strategies [1,10]. The results have suggested that the centric phase-encoding strategy causes a loss of high-frequency information, while a sequential phase-encoding tactic results in a loss in overall SNR and unequal representation of high spatial frequencies. A VFA sequence corrects for this problem as flip angles are increased to yield the same signal amplitude after each pulse, concluding with a final 90° pulse that exhausts the entire remaining polarization. Thus, the VFA scheme features constant signal amplitude across all of k-space (prior to phase encoding) and results in good spatial resolution, but at the expense of a low SNR.

Due to the application of constant-amplitude RF pulses applied during each row of the k-space acquisition, the CFA scheme causes the signal amplitude to decay nonlinearly, as can be seen from the black dotted curve in Fig. 1(a) [where T_1-relaxation is ignored]. Clearly, this method does not make optimal use of the polarization provided, as can be seen from the black dotted curve in Fig. 1(b). These curves show the theoretical hyperpolarized media signal amplitude and the relationship between the remaining hyperpolarized magnetization and the number of excitation pulses when the CFA scheme is used with a constant pulse flip angle of 13.33° and a total number of excitation pulses of 64. The nonlinear decline of signal amplitude and the underused polarization lead to degradation of the reconstructed MR image.

The blue[1] dotted curves in Fig. 1 represent the theoretical hyperpolarized media signal amplitude and the remaining hyperpolarized magnetization when the VFA scheme is used. Where the initial pulse flip angle is 7.18°, the final flip angle is 90°, and the total number of excitation pulses is 64, respectively. The VFA scheme can mitigate signal losses during the signal acquisition by gradually increasing the flip angle. It can improve the SNR and eliminate some typical artifacts of hyperpolarized media [10,23–26]. Note that the VFA scheme keeps the same signal amplitude over the course of the acquisition train. The FID (free induction decay) amplitudes acquired by using the VFA scheme are smaller than those acquired via the CFA scheme during the first 23 excitation pulses, as shown in Fig. 1(a). Wild et al. [1] have point out that a measure of SNR in the reconstructed image is the amplitude of the magnetization evaluated at the central k-space point. In addition, the initial variable pulse-flip angle used in the VFA scheme is less than the constant one used in the CVF scheme, as shown in Fig. 1, whereas too small a flip angle may result in an unacceptably low SNR [10]. Therefore, the way in which one efficiently utilizes the nonrenewable hyperpolarized magnetization will play a key role in the applications of hyperpolarized media MRI.

The purpose of this work is to present a novel small-angle-excitation method, which we term the constant-variable flip angle (CVFA) scheme. The CVFA scheme suggests that hyperpolarized MR signals are first acquired through a train of n^* CFA excitation pulses, followed by a train of N–n^* VFA excitation pulses, where N is the total number of excitation pulses. This aims at maximizing SNR while keeping fine structure details of the reconstructed image. The red dotted curves in Fig. 1 denote the theoretical hyperpolarized media signal amplitudes and the remaining hyperpolarized magnetization obtained via the CVFA scheme. Where $N = 64$, $n^* = 18$, the flip angle used in the CFA pulse process was 13.33°, and the initial and the final flip angles used in the VFA pulse process were 13.33° and 90°, respectively. Fig. 1 suggests that the CVFA scheme is a trade-off between CFA and VFA in both the signal amplitude and residual hyperpolarized magnetization.

2. Theory

2.1. CFA scheme

For hyperpolarized media MRI, the CFA scheme suggests that the transverse magnetization following the ith RF pulse obtained by Bloch equation analysis is described as [10,27],

$$S_{\mathrm{CFA}}(i) = \lambda m_0 E_1^{i-1} \sin\alpha \cos^{i-1}\alpha, \quad \text{where } E_1 = \exp(-\mathrm{TR}/T_1), \tag{1}$$

where m_0 is the thermal equilibrium longitudinal magnetization, λ is the hyperpolarization factor, α is the pulse flip angle, TR is the repetition time, and T_1 is the time constant for the hyperpolarized magnetization to relax to thermal equilibrium. Since the T_1 value of the gas in the xenon cell was quite long, T_1 relaxation effects in Eq. (1) could be ignored because of the large ratio of T_1/TR [10]. Thus, the residual longitudinal magnetization after i excitation pulses is directly proportional to the trigonometric term $\cos^i\alpha$.

In a single-echo spin warp imaging experiment, a measure of SNR in the reconstructed hyperpolarized image depends upon the magnitude of the central line of k-space [1,27]. Thus, an indication of the SNR in the image can be expressed as follows.

$$\mathrm{SNR} = C \cdot M_y/\sigma, \tag{2}$$

where C is a hardware-dependent sensitivity factor, σ is the standard deviation of the Gaussian noise distribution, and M_y is the transverse magnetization, respectively. For the centric phase encoding strategy, $M_y = \lambda m_0 \sin\alpha$, while for the sequential phase encoding strategy, $M_y = \lambda m_0 (\cos\alpha)^{n/2-1}\sin\alpha$, where n represents the number of phase-encode views, and α is the flip angle. Then, for a certain hyperpolarized media MRI, a pulse flip angle determines the acceptable SNR of the MR signal.

2.2. VFA scheme

The VFA scheme employs gradually increasing flip angles for a constant signal amplitude response over the course the acquisition train [10,23–25]. After the ith excitation pulse, the hyperpolarized transverse magnetization is

$$S_{\mathrm{VFA}}(i) = \lambda m_0 E_1^{i-1} \sin\theta(i) \prod_{k=1}^{i-1} \cos\theta(k), \tag{3}$$

where $\theta(k)$, $k = 1, 2, \ldots, i$, denotes a sequence of flip angles determined by the recursive formula: $\tan\theta(k) = E_1 \sin\theta(k+1)$. The progressive property of pulse flip angles in the VFA scheme accounts for the losses of magnetization due to RF excitation and T_1 relaxation by maintaining the constant signal amplitude [23]. The sinusoidal function $\sin\theta(k+1)$ does not exceed 1 in magnitude. If T_1 relaxation is ignored, the value of $\theta(k)$ is never greater than 45°. Thus the maximal value of $\theta(N-1)$ is 45°, where N is the total

[1] For interpretation of color in Fig. 1, the reader is referred to the web version of this article.

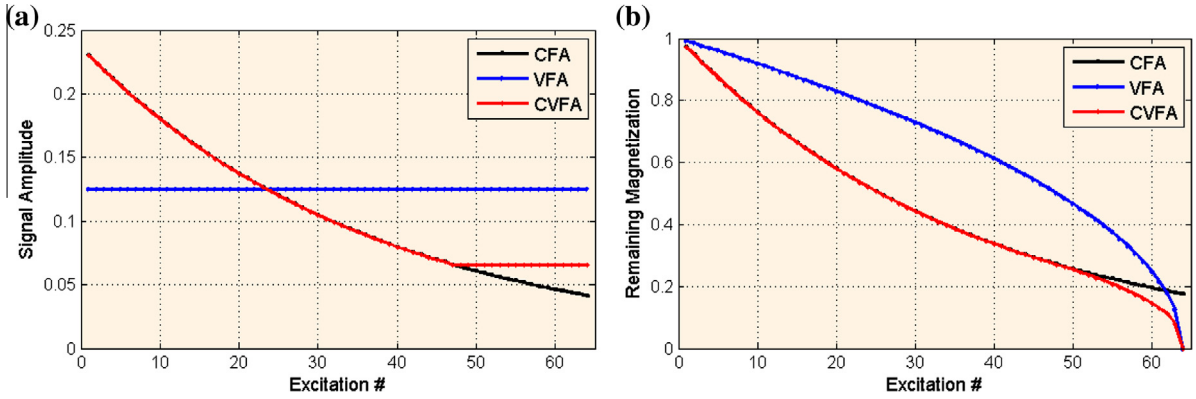

Fig. 1. (a) Theoretical hyperpolarized media signal amplitude obtained via different flip-angle pulse sequences (normalized). The total number of excitation pulses is 64. (b) Theoretical relationship between the remaining hyperpolarized magnetization and the number of excitation pulses when different flip-angle pulse sequences are used.

number of excitation pulses. Assuming $N = 64$, the maximum of the initial pulse flip angle $\theta(1)$ is 7.18° according to Eq. (3).

2.3. CVFA scheme

The proposed CVFA scheme integrates the CFA scheme together with the VFA scheme, and represents a trade-off between the two. The diagram of the CVFA scheme is shown in Fig. 2. It consists of selecting the first n^* excitation pulses as CFA pulses, followed by a sequence of N–n^* VFA excitation pulses. Here, α is the flip angle used in the CFA pulses process, $\theta^*(i)$, $i = 1, \ldots, N$–n^*, are the variable flip angles used in the VFA pulses process, and N is the total number of excitation pulses.

If the CFA excitation pulses continued indefinitely, the signal amplitude after the $(n^* + 1)$th CFA excitation pulse would be no higher than that following the first VFA excitation pulse of this sequence. Thus, we adopted to do a Bloch equation analysis using three simple assumptions to determine the parameters involved in the CVFA scheme: (1) the transverse magnetization is completely spoiled prior to each RF pulse; (2) the thermal equilibrium term is negligible; and (3) the FID amplitude after the first VFA excitation pulse is no less than that after the (n^*+1)th CFA excitation pulse, and no more than that after the n^*th CFA excitation pulse.

Based on the third assumption, the following inequalities relating FID amplitudes is satisfied,

$$S_{\mathrm{CFA}}(n^* + 1) \leqslant S_{\mathrm{VFA}}(1) \leqslant S_{\mathrm{CFA}}(n^*), \tag{4}$$

where $S_{\mathrm{CFA}}(n^*)$ or $S_{\mathrm{CFA}}(n^* + 1)$ denotes the FID amplitude after the n^*th or $(n^* + 1)$th CFA excitation pulse, and $S_{VFA}(1)$ is the FID amplitude after the first VFA excitation pulse. Thus,

$$\begin{aligned}\lambda m_0 E_1^{n^*} \sin\alpha \cos^{n^*}\alpha &\leqslant \lambda m_0 E_1^{n^*} \sin\theta^*(1) \cos^{n^*}\alpha \\ &\leqslant \lambda m_0 E_1^{n^*-1} \sin\alpha \cos^{n^*-1}\alpha,\end{aligned} \tag{5}$$

and

$$\alpha \leqslant \theta^*(1) \leqslant \sin^{-1}(E_1^{-1} \cdot \tan\alpha). \tag{6}$$

Ignoring T_1 relaxation, Eq. (6) becomes simply $\alpha \leqslant \theta^*(1) \leqslant \sin^{-1}(\tan\alpha)$. For simplicity, $\theta^*(1)$ is set to α in this paper.

According to Eq. (3), the relationship of flip angles between the kth and $(k + 1)$th excitation pulses adopted in the VFA pulses process is [if $\theta(k + 1) < 90°$],

$$\tan\theta(k) = E_1 \sin\theta(k+1) \Rightarrow \tan^2\theta(k) = E_1^2 \cdot \frac{\tan^2\theta(k+1)}{1 + \tan^2\theta(k+1)}. \tag{7}$$

Since the available hyperpolarized magnetization is limited and nonrenewable, the CVFA scheme should effectively utilize all available magnetization provided for a given N [N is the total number of excitation pulses]. This suggests that the final variable-flip angle $\theta^*(N–n^*)$ may as high as 90°. Thus, the initial variable-flip angle used in the VFA pulses process is [see Appendix],

$$\theta^*(1) = \tan^{-1}\left(E_1^{(N-n^*-1)} \cdot \left(\sum_{i=1}^{N-n^*-1} E_1^{2(i-1)}\right)^{-1/2}\right). \tag{8}$$

Eq. (8) establishes the relationship among the initial flip angles, FID amplitudes, and the number of CFA or VFA excitation pulses for hyperpolarized media MRI. If $\theta^*(1)$ is chosen as α, the values of n^*, N–n^* and $\theta^*(N–n^*)$ will be chosen when the values of N and α are given.

However, several unknown variables are involved in Eq. (8), making the solutions of the CVFA scheme non unique. In this case, for a given N, TR and T_1, we want to find a simple relationship among the flip angle α, the number of CFA excitation pulses n^*, the number of VFA excitation pulses N–n^*, the initial variable-flip angle $\theta^*(1)$, and the final variable flip angle $\theta^*(N–n^*)$. This relationship is only possible for hyperpolarized magnetization and does not apply to the thermal polarization.

Assume that the peak of the point-spread function (PSF) of the k-space signal is used to estimate the signal, and noise is proportional to the square root of the number of excitation pulses, then the SNR in the case of constant flip angle is estimated by the following expression [28].

$$\mathrm{SNR} \sim \frac{S(0)}{\sqrt{n}} \propto \frac{1}{\sqrt{n}} \sin\alpha \frac{1 - E_1^n \cos^n\alpha}{1 - E_1 \cos\alpha}, \tag{9}$$

where $S(0)$ is the peak of the PSF, α is the flip angle, and n is the number of excitation pulses, respectively. Note that Eq. (9) consists of the terms of n, α, TR and T_1.

The above function SNR suggests that for a given n there exists an optimal value of flip angle at which the SNR is maximal. The optimal value of flip angle involves a trade-off depletion of the nonrenewable hyperpolarized longitudinal magnetization and the generation of transverse magnetization. We set the derivative of the SNR in terms of α equal to zero to find the optimum flip angle, that is,

$$\begin{aligned}\frac{\partial SNR}{\partial\alpha} = 0 \Rightarrow\ & E_1^{-1}\cos^2\alpha(1 - (E_1\cos\alpha)^n) \\ & - \cos^3\alpha(1 - (E_1\cos\alpha)^n) + nE_1^{-1}(E_1\cos\alpha)^n \sin^2\alpha \\ & - \cos\alpha(1 - (E_1\cos\alpha)^n + n(E_1\cos\alpha)^n)\sin^2\alpha = 0,\end{aligned} \tag{10}$$

For a given n, the optimum flip angle α can be derived by numerically solving Eq. (10). When $\theta^*(1)$ is chosen as α, the number of VFA excitation pulses (N–n^*) is derived by numerically solving Eq. (8). Therefore, if the values of n^*, TR and T_1 are given, the

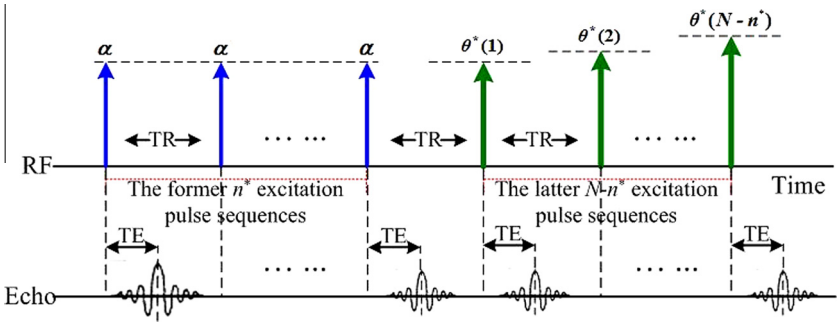

Fig. 2. Timing diagram of the CVFA scheme.

parameters, α, N–n^*, $\theta^*(1)$, and $\theta^*(N–n^*)$ will be achieved. For example, when $n^* = 32$, TR = 15 ms, and $T_1 = 12$ s, then $\alpha = \theta^*(1) = 16°$, $\theta^*(N–n^*) = 90°$, and $N–n^* = 14$.

If TR is much less than T_1 [TR $\ll T_1$], Eqs. (8) and (10) will be simplified to,

$$\tan\theta^*(1) = 1/\sqrt{N - n^* - 1}, \tag{11}$$

and

$$(\cos^2\alpha - \cos^3\alpha)(1 - \cos^n\alpha) + n\sin^2\alpha\cos^n\alpha - \cos\alpha\sin^2\alpha(1 - \cos^n\alpha + n\cos^n\alpha) = 0, \tag{12}$$

Then, the solution of α, N–n^* and $\theta^*(1)$ is independent of TR and T_1.

3. Results and discussion

3.1. Parameters solution

Since we can only achieve an implicit solution according to Eqs. (8) and (10), or Eqs. (11) and (12), the optimal parameters of the CVFA scheme can be obtained via a numerical method. Fig. 3 shows the relationship between TR/T_1 and the fraction of VFA excitation pulses in the CVFA scheme for different numbers of CFA excitation pulses. Fig. 3 shows that as TR/T_1 is reduced, the fraction of VFA excitation pulses becomes more independent of that ratio. The fraction remains at about 30% when TR is much less than T_1. This suggests that if T_1 relaxation is ignored, the number of CFA excitation pulses and the number of VFA excitation pulses can be selected for a given the total number of excitation pulses. In this case, the fraction of CFA excitation pulses is about 70%, and the rest of pulses are VFA excitation pulses. Afterwards, the initial flip angle $\theta^*(1)$ can be determined according to Eq. (11). Then, the other parameters involved in the CVFA scheme are easily obtained.

For TR = 10.37 ms and $T_1 = 7.7$ s, Table 1 lists the optimal flip angles [α] and the number of excitation pulses [n^*] adopted in the CFA pulses process, the optimal initial variable-flip angles [$\theta^*(1)$], the number of excitation pulses [N–n^*] adopted in the VFA pulses process, and the percentage of CFA excitation pulses involved in the CVFA scheme for different total numbers of excitation pulses. The final flip angles in the CVFA scheme are always 90°, regardless of the value of N. The value of N–n^* varies directly with the number of CFA excitation pulses, and inversely with the optimal flip angles [α and $\theta^*(1)$]. The fraction of CFA excitation pulses under different values of N is within an interval [0.69,0.74]. The initial flip angles [$\theta(1)$] according to Eq. (7) under N = 32, 64, 96, 120, 148, 160, 180, 210, 240, and 320 are also listed in Table 1. For N = 210, 240 and 320, the respective initial flip angle is 3.41°, 3.12° and 2.54°, which probably induces unacceptably low SNR values for hyperpolarized NMR signals because the signal strength primarily depends upon the magnitude of the central line of k-space.

When T_1 relaxation is ignored, Table 2 lists the optimal parameters involved in the CVFA scheme for different total numbers of excitation pulses. The percentages of CFA excitation pulses under different total numbers of excitation pulses are ~72%. Comparing Tables 1 and 2, most of the parameters have changed slightly. For the CFA scheme, the flip angles in Table 2 are no less than those of Table 1. While for the VFA scheme, the initial flip angles in Table 2 are larger than those in Table 1.

3.2. Accuracy

The SNR of a Fourier transform (FT) spectrum is determined by the highest data point in the reciprocal domain [viz., k-space].

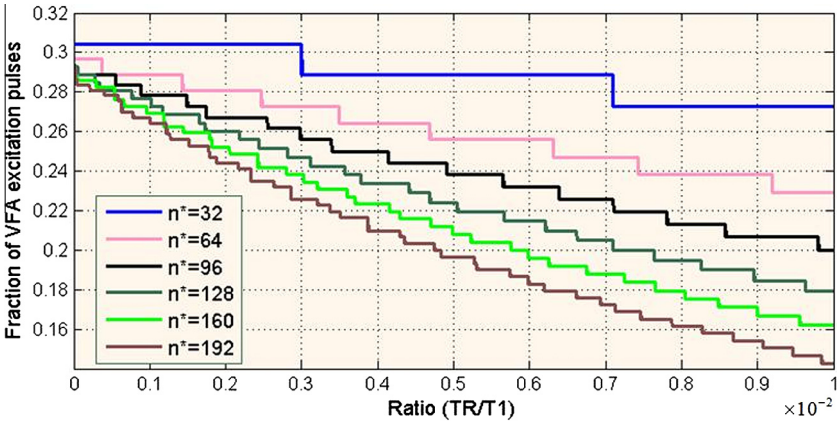

Fig. 3. The fraction of VFA excitation in whole CVFA excitation for different values of TR/T_1.

Table 1
Optimum values for α, $\theta^*(1)$ and N–n^* when TR = 10.37 ms, T_1 = 7.7 s.

N	32	64	96	120	148	160	180	210	240	320
n^*	22	45	69	86	107	116	132	154	178	240
α	19.26°	13.58°	11.03°	9.92°	8.93°	8.59°	8.08°	7.51°	7.02°	6.11°
$\theta^*(1)$	19.26°	13.58°	11.03°	9.92°	8.93°	8.59°	8.08°	7.51°	7.02°	6.11°
N–n^*	10	19	27	34	41	44	48	56	62	80
n^*/N	0.69	0.70	0.72	0.72	0.72	0.72	0.73	0.73	0.74	0.75
θ (1)	9.97°	6.88°	5.49°	4.82°	4.25°	4.06°	3.78°	3.41°	3.12°	2.54°

Table 2
Optimum values for α, $\theta^*(1)$ and N–n^* when T_1 relaxation is ignored.

N	32	64	96	120	148	160	180	210	240	320
n^*	23	46	69	86	106	115	129	150	171	229
α	18.77°	13.33°	10.90°	9.77°	8.80°	8.45°	7.98°	7.41°	6.94°	6.02°
$\theta^*(1)$	18.77°	13.33°	10.90°	9.77°	8.80°	8.45°	7.98°	7.41°	6.94°	6.02°
N–n^*	9	18	27	34	42	45	51	60	69	91
n^*/N	0.72	0.72	0.72	0.72	0.72	0.72	0.72	0.71	0.71	0.71
θ (1)	10.18°	7.18°	5.86°	5.24°	4.72°	4.53°	4.27°	3.96°	3.70°	3.20°

When the data acquisition of hyperpolarized magnetization in the CVFA scheme is started from the center of k-space, the superficial appearance of reconstructed MR image becomes good. However, the first n^* CFA excitation pulses inevitably sacrifices the accuracy of spatial information because T_1 relaxation of hyperpolarized magnetization blurs the feature in a similar fashion as exponential line-broadening. In order to qualitatively analyze the relationship between the image SNR and accuracy, we adopt a numerical simulation method to simulate the data acquisition of hyperpolarized magnetization through the CFA, VFA and CVFA schemes.

In the case of the gradient-recalled echo pulse sequence for the proton MRI, the k-space signal from the kth excitation is expressed as,

$$s_1(k) = \sum_{x=0}^{N-1} M_0(x) \exp(j2\pi kx/N), \tag{13}$$

where M_0 denotes the initial longitudinal magnetization, k denotes the excitation index, N denotes the total number of excitation pulses, $x = -N/2,\ -N/2+1, \ldots, N/2-1$ denotes the spatial pixel index, and $\exp(j2\pi kx/N)$ denotes the phase-encoding term, respectively. The frequency-encoding term in Eq. (14) is ignored for simplification.

For the hyperpolarized noble gas MRI with the CFA, VFA or CVFA scheme (centric encoding), the k-space signal from the kth excitation is,

$$\begin{aligned}
s_2(k) &= \sum_{x=0}^{N-1} M_0(x) \exp(-(k-1)TR/T_1) \cos^{k-1}\alpha \sin\alpha \exp(j2\pi kx/N) \\
s_3(k) &= \sum_{x=0}^{N-1} M_0(x) \exp(-(k-1)TR/T_1) \sin\theta(k) \exp(j2\pi kx/N) \prod_{i=1}^{k-1} \cos\theta(i) \\
s_4(k) &= \begin{cases} \sum_{x=0}^{N-1} M_0(x) \exp(-(k-1)TR/T_1) \cos^{k-1}\alpha \sin\alpha \exp(j2\pi kx/N), & \text{if } 1 \leqslant k \leqslant n^* \\ \sum_{x=0}^{N-1} M_0(x) \exp(-(k-1)TR/T_1) \cos^{n^*}\alpha \sin\theta^*(t) \exp(j2\pi kx/N) \prod_{l=1}^{t-1} \cos\theta^*(l), & \text{if } n^* < k \leqslant N \end{cases}
\end{aligned} \tag{14}$$

where $t = k-n^*$, α, $\theta(i)$, $i = 1, \ldots, N$, and $\theta^*(l)$, $l = 1, \ldots, N-n^*$, are the flip angles, n^* is the number of CFA excitation pulses adopted in the CVFA scheme, T_1 is the spin lattice relaxation time, and TR is the repetition time, respectively.

Afterwards, the k-space signal acquired by the hyperpolarized gas MRI with the CFA, VFA or CVFA schemes can be achieved approximatively from the k-space signal that acquired by proton MRI multiplied by different coefficients. The k-space data of the CFA, VFA or CVFA scheme can be expressed as follows:

$$\begin{aligned}
K_1(p,q) &= K(p,q) \cdot C_1(p,q) + K_n \\
K_2(p,q) &= K(p,q) \cdot C_2(p,q) + K_n \\
K_3(p,q) &= K(p,q) \cdot C_3(p,q) + K_n
\end{aligned} \tag{15}$$

where K_1, K_2 and K_3 denote the k-space data of the CFA, VFA and CVFA schemes, K denotes the k-space data of the proton MRI, K_n denotes the noise, (p,q) denotes the spatial pixel index, and C_1, C_2 and C_3 denote the coefficient matrices, respectively. We find that $C_1(p,q) = \cos^{p-1}\alpha \ \sin\alpha$, $C_2(p,q) = \sin\theta(p)\Pi_{i=1,\ldots,\ p-1} \ \cos\theta(i)$, and $C_3(p,\ q) = \cos^{p-1}\alpha \ \sin\alpha$ (if only p was no more than n^*) or $C_3(p,q) = \cos^{n*}\alpha \ \sin\theta^*(p-n^*)\Pi_{l=1,\ldots,\ p-n*-1}\cos\theta(l)$ (others). When T_1 relaxation is ignored, the flip angles [α, $\theta(i)$ and $\theta^*(l)$] are defined in Table 2. Moreover, we assume that there exists similar noise types involved in the CFA, VFA and CVFA schemes, and K_n is assumed to be complex white Gaussian noise.

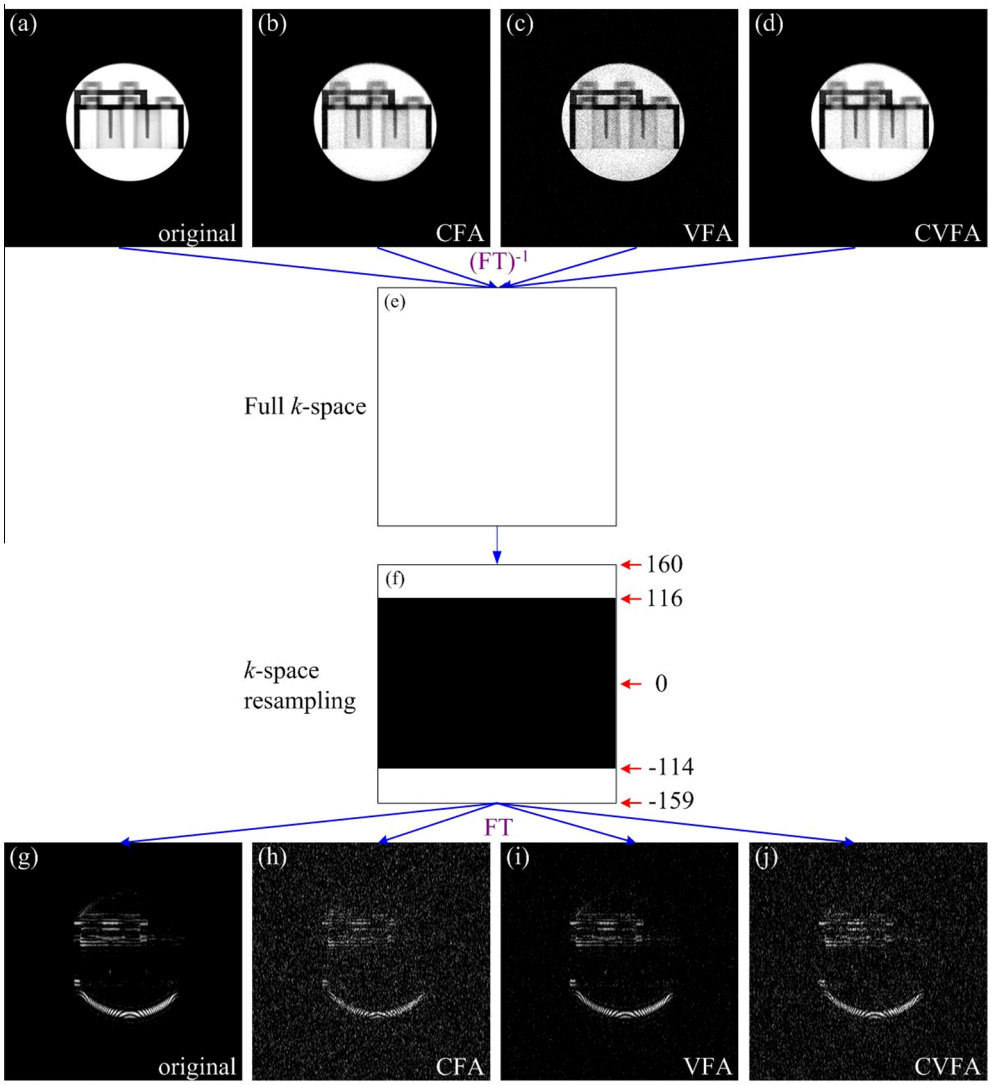

Fig. 4. Comparison images with full *k*-space and *k*-space resampling by different schemes. (a) The original high quality proton image of a water phantom. (b)–(d) Reconstructed images obtained by using CFA, VFA and CVFA schemes based on the original *k*-space data of (a). (e) Full *k*-space by the inverse Fourier transform from the original images. (f) *k*-space resampling with lines [160: 116] and [−114: −159] of (e), and the other lines are zero filled, in order to keep the high frequency signal at the periphery of the *k*-space. (g)–(j) Corresponding images reconstructed from (a)–(d) by resampling with (f), showing the fine structure details of the phantom by different schemes.

Fig. 4(a) shows a proton MR image of a water phantom acquired on the 1.5 Tesla (T) clinical scanner (Siemens). The pulse sequence used to acquire this image was a gradient echo sequence (2D FLASH) with echo time (TE) = 9.8 ms, TR = 20.0 ms, bandwidth = 3.2 kHz, matrix size = 320 × 320, field of view (FOV) = 52 × 52 mm^2, slick thickness = 20 mm, and number of averages = 100. According to Eq. (15), the corresponding reconstructed images obtained by using CFA, VFA and CVFA schemes are shown in Fig. 4(b)–(d). Where the high intensity noise was adopted in the computation of the reconstructed images. The original proton image and reconstructed images were processed using the same contrast level and gray scale window.

Since the edges of *k*-space represent the fine structure details of an image, we adopt a portion of *k*-space data to reconstruct MR images, aiming to compare the accuracy obtained by using different pulse sequences. The low intensity noise was adopted in this experiment. We selected line 160–116 and line −114 to −159 of *k*-space data, as shown in Fig. 4(f). The reconstructed MR images are shown in Fig. 4(g)–(j). The SNR of the reconstructed MR image is the ratio of the mean of the signal magnitude over the standard deviation of the noise [29]. The mean of the signal is estimated in a region of the image where the signal is strong, while the noise is estimated in a region of no signal. The SNR values of Fig. 4(b)–(d) are 263.28, 35.80, and 218.33, and the SNR values of Fig. 4(g)–(j) are 5.16, 16.88 and 6.48, respectively. From Fig. 4, it can be found that the VFA images achieve high accuracy but low SNR, while the CFA images maintain high SNR but low accuracy. However, the CVFA images can keep high SNR values and accuracy [see Fig. 4 (d) and (j)]. Therefore, there is a compromise between the SNR and accuracy using the CVFA scheme.

3.3. Phantom

A homebuilt 8-leg birdcage radiofrequency coil tuned to ^{129}Xe (83.07 MHz) frequency was used in MRI experiments that were acquired from the 7.0 T scanner (BioSpec 70/20USR, Bruker). Hyperpolarized ^{129}Xe gas (26.4% natural abundance) was polarized by a homebuilt continuous-flow SEOP polarizer, producing a polarization of about 10%. Then, hyperpolarized gases were delivered

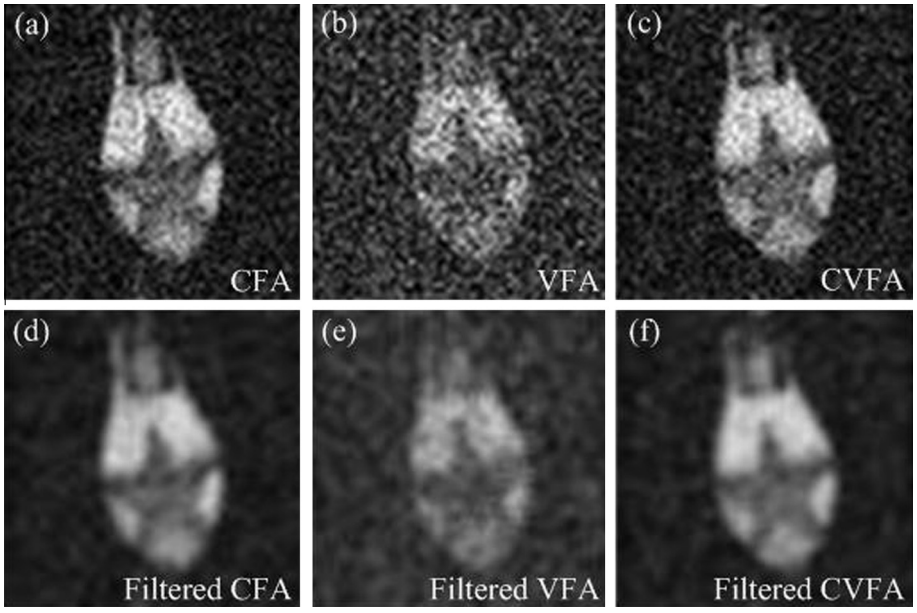

Fig. 5. A solid plastic pentangle phantom: (a)–(c) Hyperpolarized ^{129}Xe gradient-echo images obtained by using CFA, VFA and CVFA schemes. (d)–(f) Corresponding filtered results of (a)–(c).

into a balloon by a homebuilt ventilator, and the tidal volume per imaging was about 3 ml.

Fig. 5(a)–(c) shows hyperpolarized ^{129}Xe MR images of a balloon obtained via the CFA, VFA and CVFA schemes when T_1 relaxation was ignored [2D spoiled gradient-echo sequence was used, where TE = 1.8 ms, TR = 100 ms, matrix size = 64 × 64, number of slices = 1, slice thickness = 10 cm, FOV = 5 × 5cm^2, bandwidth = 50 kHz, centric k-space ordering along the phase encode direction, total scan time = 6.4 s]. A solid plastic pentangle phantom was set inside the balloon. The selection of slice thickness was to cover the whole balloon and phantom in the MR images. According to Table 2, the flip angle used in the CFA scheme was set to 13.33°, the initial flip angle used in the VFA scheme was set to 7.18°, and both the constant flip angle (α) and the initial variable-flip angle [$\theta^*(1)$] used in the CVFA scheme were set to 13.33°.

Hyperpolarized ^{129}Xe NMR signals acquired by the CFA, VFA and CVFA schemes are shown in Fig. 6 [TR = 100 ms, matrix size = 1024 × 1, bandwidth = 25 kHz]. After receiving the NMR FIDs, a dephase gradient was applied in the read orientation at the end of each repetition. The NMR FIDs were transformed to complex Lorentzian spectrums by Fourier transform, followed by phase correction. Spectral peaks were at the position of 0 ppm in the absorption Lorentzian. We chose the integral range from −15 ppm to 15 ppm in the absorption Lorentzian lineshape as the signal amplitude.

The respective SNR values of the images [i.e., Fig. 5(a)–(c)] are 17.61, 10.37 and 18.20. The SNR value of Fig. 5(b) is the lowest, while the SNR value of Fig. 5(a) is almost equal to that of Fig. 5(c). As for the outline resolution of the pentangle phantom, Fig. 5(b) is best, while Fig. 5(a) is the poorest. However, the resolution difference of the outline of the pentangle phantom between Fig. 5(a) and (c) is inferior to that between Fig. 5(a) and (b). The reason may due to the relatively low signal amplitudes of the last 18 excitations obtained via the CVFA scheme. In order to better compare the image quality, these images are filtered by a suitable denoising algorithm, and the filtered results are shown in Fig. 5(d)–(f). The SNR values of Fig. 5(d)–(f) are 23.61, 12.72, and

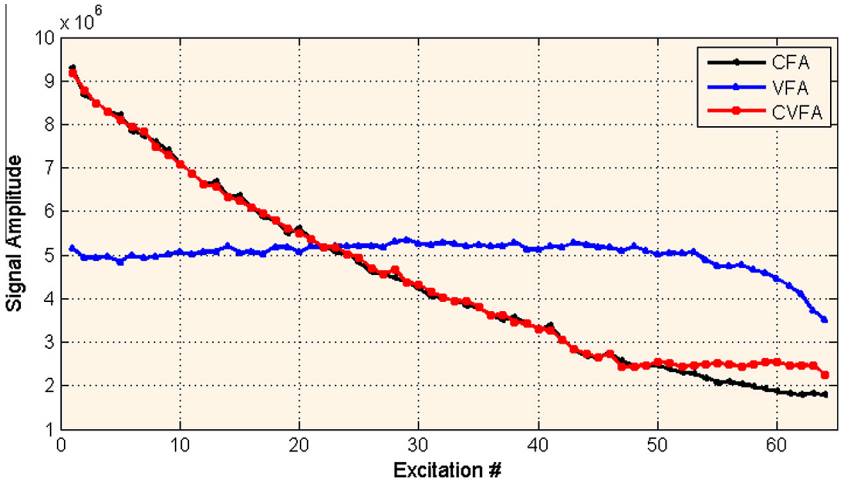

Fig. 6. Hyperpolarized ^{129}Xe signal amplitude obtained via CFA, VFA and CVFA schemes.

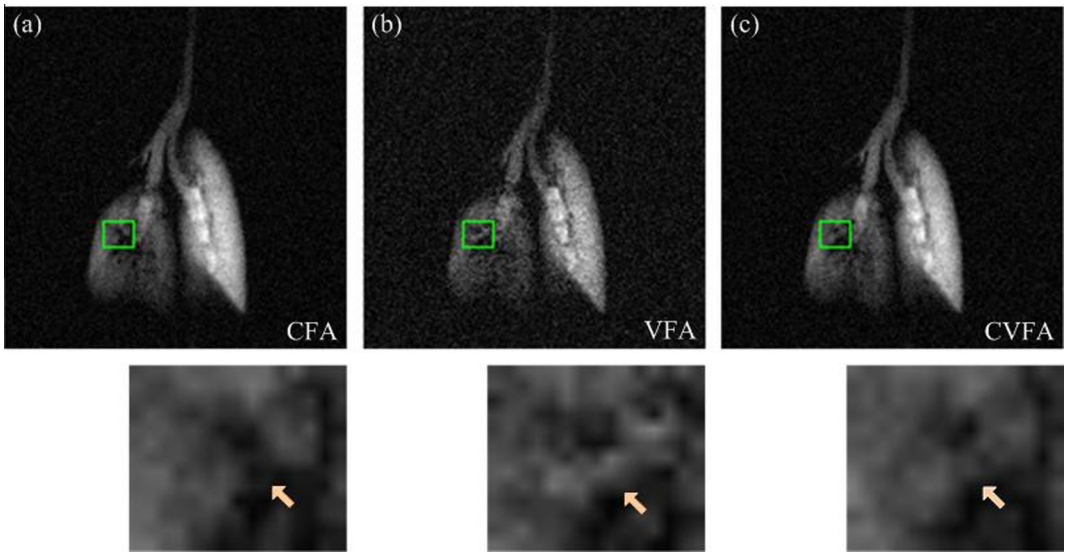

Fig. 7. 2D gradient-echo *in vivo* ^{129}Xe lung MR images of a rat (upper) and the zoom-in ROIs of green rectangles (lower). (a)–(c) Lung images obtained by using CFA, VFA and CVFA schemes, respectively. The CFA image does not clearly show the ventilation at the arrowed pixels, however the VFA image gives the detailed structure information, demonstrating not a ventilation defect. The CVFA image can also visualize such ventilation details as well as keeping a high SNR.

21.99. The comparisons derived from Fig. 5 suggest that with the centric encoding strategy, the CVFA scheme can maintain a high SNR while preserving fine structure details.

As shown in Fig. 6, the signal amplitudes of 64 excitation pulses obtained via the VFA scheme are almost even [mean/SD = $5.1 \times 10^6/0.15 \times 10^6$, and the fluctuation is just 3%, where SD is the standard deviation] except for the final 6 pulses. Whereas, the signal amplitudes of the whole 64 pulses obtained via the CFA scheme are proportional to $(\cos\theta)^n$, where θ is the pulse flip angle. The signal amplitudes of the former 46 excitation pulses acquired by the CVFA scheme are almost the same as those acquired by the CFA scheme, and the latter 18 pulses are nearly flat [mean/SD = $2.9 \times 10^6/0.06 \times 10^6$, and the fluctuation is 2%]. Owing to unavoidable inhomogeneities of B_1 field (magnetic field associated with RF) and ignoring T_1 relaxation, the signal amplitudes of the final 2 pulses obtained via the CVFA scheme trend to decrease, as well as the signal amplitudes of the final 6 pulses obtained via the VFA scheme. The signal amplitudes of the former 22 pulses acquired by the VFA scheme are smaller than those acquired by the CFA and CVFA schemes, which leads to the lowest SNR value, as shown in Fig. 5(b). Meanwhile, the signal amplitudes of final 42 pulses obtained via the VFA scheme are higher than those obtained via the CFA and CVFA schemes, which provides the highest outline resolution of the pentangle phantom. After comparing the CVFA scheme with the CFA scheme, we find that the former 46 same excitation pulses produce almost the same SNR value. And the higher signal amplitudes of the latter 18 pulses acquired by the CVFA scheme resulted in the higher resolution of boundaries of images of the pentangle phantom. In other words, the sum of signal amplitudes obtained via the CVFA scheme is greater than those obtained via the CFA scheme, which suggests that the consumption rate of polarization using the CVFA scheme is lower than that of the CFA scheme.

3.4. In vivo

The above plastic pentangle phantom results do not completely confirm the superiority of the CVFA scheme in hyperpolarized noble gas MRI. The reason is that the relatively low polarization used and the slice thickness chosen in our experiments lead to little fine structure details of the images. Comparing the phantoms used in our experiments with *in vivo* results, we find that relatively more detailed information is contained in lungs or brains *in vivo*.

Fig. 7 shows hyperpolarized ^{129}Xe MR images of a rat lung obtained by using the CFA, VFA and CVFA schemes. These *in vivo* experiments were performed with a Sprague Dawley rat (143 g weight), where the ventilation parameters were the same as that adopted in the phantom experiments. The anesthesia was induced with 5% isoflurane and maintained with 2% isoflurane. A 14 G endotracheal tube was intubated, and tied to the trachea of rat. The MRI parameters were: TE = 3 ms, TR = 10.37 ms, T_1 = 7.7 s, matrix size = 160×160, FOV = 55×55 mm^2, slice thickness = 35 mm, bandwidth = 30 kHz. In addition, the T_1 relaxation of ^{129}Xe gas in rat lung was measured beforehand. According to Table 1, the flip angle used in the CFA scheme was 8.59°, the initial flip angle used in the VFA scheme was 4.06°. And the CVFA scheme adopted the first 116 pulses were CFA excitation pulses [the flip angle was set to 8.59°], followed by the final 44 pulses, which were VFA excitation pulses [the initial flip angle was 8.59° and the final flip angle was 90°].

The SNR values of Fig. 7(a)–(c) are 30.86, 16.89 and 28.69, respectively. The green rectangles in Fig. 7 indicate the regions of interest (ROIs), and they are shown in the lower row of Fig. 7. Fig. 7(b) can provide more fine structure details than Fig. 7(a), despite that it contains much noise. The conclusion derived from Fig. 7 with regards to the SNR and image details is similar to that derived from Figs. 4–6, that is, the CVFA scheme can improve the image quality.

4. Conclusion

In conclusion, we propose a constant-variable flip angle (CVFA) scheme to effectively utilize the non-equilibrium spin polarization of hyperpolarized media, in order to achieve a high SNR as well as keep the fine structure details of MR image. The CVFA scheme takes advantages of both CFA and VFA schemes by intelligently allocating hyperpolarized magnetization over the *k*-space during the acquisition. Hyperpolarized ^{129}Xe MRI *in vivo* experiment demonstrated the efficacy of the CVFA scheme in the lung ventilation image. This method should be also helpful for other hyperpolarized media MRI applications.

Acknowledgments

This work was supported by the Natural Science Foundation of China (81227902 and 61471355) and the China Postdoctoral Science Foundation (2014M560636 and 2015T80856).

Appendix A

Because the final variable-flip angle $\theta^*(N–n^*)$ is set as 90° in the CVFA scheme, then the following formula is tenable according to Eq. (7).

$$\tan^2\theta^*(N-n^*-1)=E_1^2, \tag{16}$$

After that,

$$\begin{aligned}\tan^2\theta^*(N-n^*-2)&=\frac{E_1^4}{1+E_1^2},\tan^2\theta^*(N-n^*-3)\\&=\frac{E_1^6}{1+E_1^2+E_1^4},\tan^2\theta^*(N-n^*-4)\\&=\frac{E_1^8}{1+E_1^2+E_1^4+E_1^6},\dots\end{aligned} \tag{17}$$

Then

$$\begin{aligned}\tan^2\theta^*(1)&=\frac{E_1^{2(N-n^*-1)}}{1+E_1^2+E_1^4+\cdots+E_1^{2(N-n^*-2)}}\Rightarrow\theta^*(1)\\&=\tan^{-1}\left(E_1^{N-n^*-1}\cdot\left(\sum_{i=1}^{N-n^*-1}E_1^{2(i-1)}\right)^{-1/2}\right)\end{aligned}$$

References

[1] J.M. Wild, M.N. Paley, M. Viallon, W.G. Schreiber, E.J. van Beek, P.D. Griffiths, K-space filtering in 2D gradient-echo breath-hold hyperpolarized ^{3}He MRI: spatial resolution and signal-to-noise ratio considerations, Magn. Reson. Med. 47 (2002) 687–695.

[2] Z. Liu, T. Araki, Y. Okajima, M. Albert, H. Hatabu, Pulmonary hyperpolarized noble gas MRI: recent advances and perspectives in clinical application, Eur. J. Radiol. 83 (2014) 1282–1291.

[3] M.S. Albert, G.D. Cates, B. Driehuys, W. Happer, B. Saam, C.S. Springer Jr., A. Wishnia, Biological magnetic resonance imaging using laser-polarized ^{129}Xe, Nature 370 (1994) 199–201.

[4] S. Matsuoka, S. Patz, M.S. Albert, Y. Sun, R.R. Rizi, W.B. Gefter, H. Hatabu, Hyperpolarized gas MR imaging of the lung: current status as a research tool, J. Thorac. Imaging 24 (2009) 181–188.

[5] S. Fain, M.L. Schiebler, D.G. McCormack, G. Parraga, Imaging of lung function using hyperpolarized helium-3 magnetic resonance imaging: review of current and emerging translational methods and applications, J. Magn. Reson. Imaging 32 (2010) 1398–1408.

[6] D.J. Niles, S.J. Kruger, B.J. Dardzinski, A. Harman, N.N. Jarjour, M. Ruddy, S.K. Nagle, C.J. François, S.B. Fain, Exercise-induced bronchoconstriction: reproducibility of hyperpolarized ^{3}He MR imaging, Radiology 266 (2013) 618–625.

[7] N. Graham, R.P. Steven, X.J. Xu, P.R. Juan, M.W. Jim, Optimized production of hyperpolarized ^{129}Xe at 2 bars for *in vivo* lung magnetic resonance imaging, J. Appl. Phys. 113 (2013). 044908-1-9.

[8] J.P. Mugler III, T.A. Altes, Hyperpolarized ^{129}Xe MRI of the human lung, J. Magn. Reson. Imaging 37 (2013) 313–331.

[9] S.B. Fain, F.R. Korosec, J.H. Holmes, R. O'Halloran, R.L. Sorkness, T.M. Grist, Functional lung imaging using hyperpolarized gas MRI, J. Magn. Reson. Imaging 25 (2007) 910–923.

[10] L. Zhao, R. Mulkern, C.H. Tseng, D. Williamson, S. Patz, R. Kraft, R.L. Walsworth, F.A. Jolesz, M.S. Albert, Gradient-echo imaging considerations for hyperpolarized ^{129}Xe MR, J. Magn. Reson. Ser. B 113 (1996) 179–183.

[11] D.C. Hall, D.C. Maus, G.J. Gerfen, S.J. Inati, L.R. Becerra, F.W. Dahlquist, R.G. Griffin, Polarization-enhanced NMR spectroscopy of biomolecules in frozen solution, Science 276 (1997) 930–932.

[12] R.E. Hurd, Y.F. Yen, A. Chen, J.H. Ardenkjaer-Larsen, Hyperpolarized ^{13}C metabolic imaging using dissolution dynamic nuclear polarization, J. Magn. Reson. Imaging 36 (2012) 1314–1328.

[13] K. Golman, O. Axelsson, H. Jhannesson, S. Mansson, C. Olofsson, J.S. Petersson, Parahydrogen-induced polarization in imaging: subsecond ^{13}C Angiography, Magn. Reson. Medicine 46 (2001) 1–5.

[14] G. Collier, T. Palasz, A. Wojna, B. Glowacz, M. Suchanek, Z. Olejniczak, T. Dohnalik, A high-field ^{3}He metastability exchange optical pimping polarizer operating in a 1.5T medical scanner for lung magnetic resonance imaging, J. Appl. Phys. 113 (2013). 204905-1-9.

[15] R. Kaptein, K. Dijkstra, K. Nicolay, Laser photo-CIDNP as a surface probe for proteins in solution, Nature 274 (1978) 293–294.

[16] Y. Feng, T. Theis, X. Liang, Q. Wang, P. Zhou, W.S. Warren, Storage of hydrogen spin polarization in long-lived $^{13}C_2$ singlet order and implications for hyperpolarized magnetic resonance imaging, J. Am. Chem. Soc. 135 (2013) 9632–9635.

[17] Y. Feng, R.M. Davis, W.S. Warren, Accessing long-lived nuclear singlet states between chemically equivalent spins without breaking symmetry, Nature Phys. 8 (2012) 831–837.

[18] C.R. Bowers, D.P. Weitekamp, Parahydrogen and synthesis allow dramatically enhanced nuclear alignment, J. Am. Chem. Soc. 109 (1987) 5541–5542.

[19] T.C. Eisenschmid, R.U. Kirss, P.P. Deutsch, S.I. Hommeltoft, R. Eisenberg, J. Bargon, R.G. Lawler, A.L. Balch, Para-hyfrogen-induced polarization in heterogeneous hydrogenation reactions, J. Am. Chem. Soc. 109 (1987) 8089–8091.

[20] R. Sharma, L.S. Bouchard, Strongly hyperpolarized gas from parahydrogen by rational design of ligand-capped nanoparticles, Sci. Rep. 2 (277) (2012) 1–9.

[21] S.G. Gloeggler, A.M. Grunfeld, Y.N. Ertas, J. McCormick, S. Wagner, P.P.M. Schleker, L.S. Bouchard, Nanoparticle catalyst for heterogeneous phase para-hydrogen-induced polarization in water, Angew. Chem. Intl. Ed. 54 (2015) 2452–2456.

[22] N.N. Jarenwattananon, S. Gloeggler, T. Otto, A. Melkonian, W. Morris, S.R. Burt, O.M. Yaghi, L.S. Bouchard, Thermal maps of gases in heterogeneous reactions, Nature 502 (2013) 537–540.

[23] Y. Xing, G.D. Reed, J.M. Pauly, A.B. Kerr, P.E.Z. Larson, Optimal variable flip angle schemes for dynamic acquisition of exchanging hyperpolarized substrates, J. Magn. Reson. 234 (2013) 75–81.

[24] K. Nagashima, Optimum pulse flip angles for multi-scan acquisition of hyperpolarized NMR and MRI, J. Magn. Reson. 190 (2008) 183–188.

[25] M.H. Deppe, J.M. Wild, Variable flip angle schedules in bSSFP imaging of hyperpolarized noble gases, Magn. Reson. Med. 67 (2012) 1656–1664.

[26] A.V. Ouriadov, W.W. Lam, G.E. Santyr, Rapid 3-D mapping of hyperpolarized ^{3}He spin-lattice relaxation times using variable flip angle gradient echo imaging with application to alveolar oxygen partial pressure measurement in rat lungs, Magn. Reson. Mater. Phys. 22 (2009) 309–318.

[27] S. Ajraoui, K.J. Lee, M.H. Deppe, S.R. Parnell, J. Parra-Robles, J.M. Wild, Compressed sensing in hyperpolarized ^{3}He lung MRI, Magn. Reson. Med. 63 (2010) 1059–1069.

[28] R.F. Lee, G. Johnson, R.I. Grossman, B. Stoeckel, R. Trampel, G. McGuinness, Advantages of parallel imaging in conjunction with hyperpolarized Helium – a new approach to MRI of the lung, Magn. Reson. Med. 55 (2006) 1132–1141.

[29] L. Zhao, A.K. Venkatesh, M.S. Albert, L.P. Panych, Signal-to-noise ratio comparison of encoding methods for hyperpolarized noble gas MRI, J. Magn. Reson. 148 (2001) 314–326.